Journal of Sound and Vibration (1998) **211**(1), 95–121

THE ONE-DIMENSIONAL BENDING WAVE COUNTERPART TO THE ACOUSTIC HORN AND THE SEMI-INFINITE WEDGE

B. A. T. PETERSSON

*Department of Aeronautical and Automotive Engineering, Loughborough University, LE*11 3*TU, England*

AND

E. J. M. NIJMAN

Centro Ricerche Fiat, Strada Torino 50, 10043 *Orbassano* (*Torino*), *Italy*

(*Received* 2 *May* 1997, *and in final form* 15 *October* 1997)

The implications of spatially varying structural properties for flexural vibrations have been addressed for one-dimensional waveguides. A solution of the governing differential equation, based on Bessel functions, enables closed form expressions to be obtained for the point and transfer dynamic characteristics of finite length, tapered beams. Also, under the assumption of pure bending, a closed form expression has been derived for the semi-infinite wedge, which is valid under the same conditions as the finite case solution and which can be simply extended to encompass spatial variations obeying non-integer power laws. The influence of tapering on the energy flow is analysed for the flexural wave counterpart to the acoustic horn, constituted by a finite length taper attached to a semi-infinite, uniform beam. It is found that the main distinction to the uniform case is a comparatively broad-banded transition from flexural vibrations governed by the properties of the deep part of the system to vibrations governed by those of the slender part. The transition region is featured by a stiffness controlled initial part, followed by a resonant one. It is also found that the transition in itself involves a global resonance on which is superimposed the constructive and destructive interferences due to reflections from the discontinuity between the two structural members. On the basis of the complete expressions for the configurations studied, an estimation procedure for the mobility is proposed, which is experimentally confirmed to describe correctly the parameter influence.

1. INTRODUCTION

Over time, with an increased emphasis on lightweight and cost efficient designs, spatially varying material properties or geometry have become important aspects for many engineering applications. This trend has particular implications for the structural acoustic performance, which often is directly governed by the dynamic characteristics of a wave-carrying structure and where, for example, mass reductions imply enhanced vibrations.

Owing to the comparatively strong coupling between the bending wave motion and an ambient fluid, this wave type is especially significant for the structural acoustic performance. Accordingly, much attention has been paid the analysis of the flexural characteristics of structural elements, and theoretical frameworks for sound and vibration transmission and propagation have been developed, see e.g. references [1–3]. Rigorous analysis and calculation of the flexural characteristics, conventionally interpreted in terms

0022–460X/98/110095 + 27 $25.00/0/sv971365

of mobilities, is usually extremely difficult and numerical methods such as FE techniques must be employed. In turn, this means that detailed specifications are required of the structural system to provide the necessary input data, something which is hard to fulfil at an early stage of design. As a consequence, the computational results will be uncertain from a physical point of view [4]. Moreover, the computational effort will be overwhelming for most cases if, as is generally required, the audible frequency range is to be comprised.

At a planning or design stage, however, the numerical precision is frequently of subordinate importance. It is far more important to be able to assess the adequacy, in the physical sense, of design and noise control strategies to reach the aims specified. A physically correct description of the structural acoustic behaviour of built-up systems can often be obtained by using wave theoretical models involving elementary systems [5–7], which are combined in such a way that the governing physical phenomena of the real system are represented [8, 9]. At present, such models offer the analyst and designer versatile tools as long as structural elements with constant parameters can be assumed. For optimization purposes, however, spatially varying structural parameters are attractive, but the structural acoustic significance and influence of such variations are insufficiently clarified.

The flexural vibration of beams and plates with varying cross-sections has received substantial attention from the work of Kirchhoff and onwards (see e.g. references [10–13]) but the structural acoustic aspects have not been considered correspondingly. On the basis of a wave theoretical consideration for structures having spatially varying parameters, some of the implications are exemplified herein for the practically important case of a linearly tapered beam. The implications are viewed in terms of mobilities owing to their close relation to energy flow. From the theoretical and numerical analysis, also, an estimation procedure is proposed for this structural element, which conforms to those presented in reference [6].

2. THEORY

2.1. THE GENERAL DIFFERENTIAL EQUATION

According to Euler–Bernoulli beam theory, the equation of motion of a beam in bending is

$$\frac{\partial^2}{\partial x^2}\left(B\frac{\partial^2 V}{\partial x^2}\right) + m'\frac{\partial^2 V}{\partial t^2} = 0, \tag{1}$$

where V is the transverse velocity, B is the bending stiffness and m' the mass per unit of length (a list of symbols and notations is given in Appendix V). By substituting into it a solution with harmonic time dependence,

$$V(x, t) = v(x)\,\mathrm{e}^{\mathrm{i}\omega t}, \tag{2}$$

the differential equation is transformed into (henceforth the $\mathrm{e}^{\mathrm{i}\omega t}$ term will be suppressed for brevity),

$$\frac{\mathrm{d}^2}{\mathrm{d}x^2}\left(B\frac{\mathrm{d}^2 v}{\mathrm{d}x^2}\right) - m'\omega^2 v = 0 \tag{3}$$

If B and m' are variable along the beam, exact solutions exist provided that B and m' can be expressed by suitable functions of x. An exhaustive overview of exact solutions of equation (3) has been presented by Cranch and Adler [14]. Here focus is put on solutions

in terms of Bessel functions, as they allow for a large assortment of shape and material property variations.

It can be shown [14] that equation (3) has exact solutions in terms of Bessel functions if

$$m' = \tau_1 x^n \qquad B = \tau_2 x^{n+2}, \tag{4a,b}$$

where τ_1 and τ_2 are arbitrary constants. If the conditions in equations (4) are fulfilled, the solution of equation (3) may be expressed as

$$v(x) = x^{-n/2}(c_1 \mathrm{J}_n(2\kappa\sqrt{x}) + c_2 \mathrm{J}_{-n}(2\kappa\sqrt{x}) + c_3 \mathrm{I}_n(2\kappa\sqrt{x}) + c_4 \mathrm{I}_{-n}(2k\sqrt{x})) \tag{5a}$$

if n is not an integer, whereas for integer values of n the solution is,

$$v(x) = x^{-n/2}(c_1 \mathrm{J}_n(2\kappa\sqrt{x}) + c_2 \mathrm{Y}_n(2\kappa\sqrt{x}) + c_3 \mathrm{I}_n(2\kappa\sqrt{x}) + c_4 \mathrm{K}_n(2\kappa\sqrt{x}) \tag{5b}$$

with, for both cases, $\kappa^4 = \tau_1 \omega^2/\tau_2$. Beams that comply with the conditions given by equations (4) all display a velocity field according to equations (5).

The requirements expressed by equations (4) may be met in many different ways; for instance, by keeping the material properties constant and varying the cross section along the beam. For rectangular cross sections this results in beams which must in any case have a linear depth taper, but where the width variation may take on any power of x. Other possibilities are to fix the beam shape and vary the material properties along the beam or else to vary both material properties and cross-section dimensions. In the case of a beam with a rectangular cross-section and a linear depth variation but a non-homogeneous beam material, it may easily be verified that the density, ρ, and Young's modulus, E, must vary with the same power of x, e.g., extruded material. Bessel function solutions similar to those of equation (5) can also be found for quadratic depth and any power of width variation and for cubic depth and any power of width variation [14].

In the following, the focus is on beams with constant width and a linear depth taper, as they are prominent from a practical point of view. Furthermore, they are expected to exhibit all the basic features related to bending vibrations of variable section beams. Although not treated here, the extension of the theory to beams with linear depth taper, and any (integer) power width taper (e.g., pyramids) may be achieved in an analogous way.

2.2. THE FINITE TAPERED BEAM

Consider a finite beam with a rectangular cross-section of constant width b and a depth that varies linearly between h_0 at $x = 0$ and h_1 at $x = L$, see Figure 1. It is further assumed that the beam is made of an homogeneous linear elastic material.

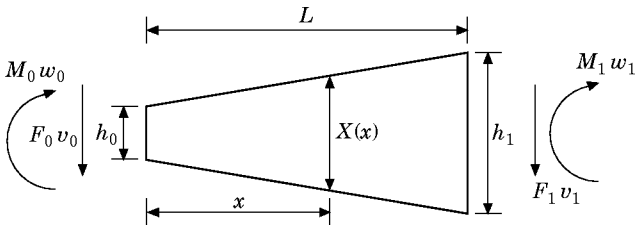

Figure 1. A finite tapered beam with the adopted notation.

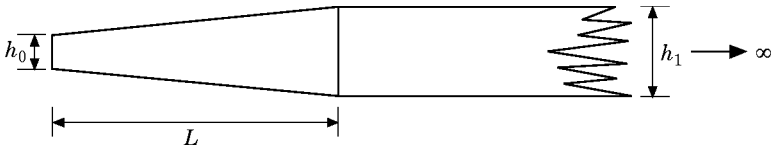

Figure 2. A semi-infinite prismatic beam with a tapered tip.

The depth X of the beam is a function of the longitudinal co-ordinate x and may be expressed as,

$$X(x) = h_0 + \alpha x, \tag{6a}$$

with

$$\alpha = (h_1 - h_0)/L. \tag{6b}$$

The mass per unit of length and the bending stiffness are consequently given by

$$m' = \rho b X \qquad \text{and} \qquad B = EI = EbX^3/12, \tag{7a, b}$$

respectively. By using equation (6), equation (3) may be rewritten as

$$\frac{\mathrm{d}^2}{\mathrm{d}X^2}\left(B\frac{\mathrm{d}^2 v}{\mathrm{d}X^2}\right) - (m'/\alpha^4)\omega^2 v = 0. \tag{8}$$

The beam depth has now become the independent variable. According to the previous section, equation (8) has a general solution equivalent to equation (5b): that is,

$$v(X) = (1/\sqrt{X})\,(c_1\,\mathrm{J}_1\,(2\kappa\sqrt{X}) + c_2\,\mathrm{Y}_1\,(2\kappa\sqrt{X}) + c_3\,\mathrm{I}_1\,(2\kappa\sqrt{X}) + c_4\,\mathrm{K}_1\,(2\kappa\sqrt{X})), \tag{9a}$$

with

$$\kappa^4 = 12\rho\omega^2/E\alpha^4. \tag{9b}$$

The four unknown (frequency dependent) coefficients c_1, c_2, c_3 and c_4 can be determined from the four boundary conditions at the beam ends. Closed form expressions can therefore be derived for every single element of the finite tapered beam impedance matrix. This impedance matrix can be formally written as

$$\begin{Bmatrix} F_0 \\ M_0 \\ F_1 \\ M_1 \end{Bmatrix} = \begin{bmatrix} Z_{00}^{Fv} & Z_{00}^{Fw} & Z_{01}^{Fv} & Z_{01}^{Fw} \\ Z_{00}^{Mv} & Z_{00}^{Mw} & Z_{01}^{Mv} & Z_{01}^{Mw} \\ Z_{10}^{Fv} & Z_{10}^{Fw} & Z_{11}^{Fv} & Z_{11}^{Fw} \\ Z_{10}^{Mv} & Z_{10}^{Mw} & Z_{11}^{Mv} & Z_{11}^{Mw} \end{bmatrix} \begin{Bmatrix} v_0 \\ w_0 \\ v_1 \\ w_1 \end{Bmatrix}, \tag{10}$$

in which the subscripts refer to the junctions, whereas the superscripts refer to the components of excitation and motion respectively. The elements of the impedance matrix (symmetric, because of reciprocity), obtained after lengthy manipulations, are given in Appendix I. For a very small taper angle, α, the impedance elements of Appendix I approximate, as expected, the so-called Kolousek beam functions [15]. This is shown in Appendix II for the driving point impedance Z_{00}^{Ev}.

2.3. THE SEMI-INFINITE PRISMATIC BEAM WITH TAPERED TIP: THE BENDING WAVE HORN

The semi-infinite beam with a uniform cross-section, equipped with a tapered tip, is shown in Figure 2. The cross-sections at the beam–tip interface are identical. This configuration represents the bending wave equivalent of the horn, because of the gradual

transition between the tip impedance and that of the semi-infinite beam. Henceforth this system will be referred to as the "bending wave horn". The impedance matrix describing the bending wave horn is obtained by adding

$$\mathbf{Z}_\infty = \begin{bmatrix} 0 & 0 & 0 & 0 \\ 0 & 0 & 0 & 0 \\ 0 & 0 & \dfrac{B_\infty k_\infty^3}{\omega}(1+\mathrm{i}) & \dfrac{B_\infty k_\infty^2}{\omega} \\ 0 & 0 & \dfrac{B_\infty k_\infty^2}{\omega} & \dfrac{B_\infty k_\infty}{\omega}(1-\mathrm{i}) \end{bmatrix} \tag{11}$$

to the impedance matrix in equation (10), where k_∞ and B_∞ are the bending wavenumber and the bending stiffness, respectively, of the prismatic semi-infinite beam. Note that the characteristic beam impedances in the matrix of equation (11) consist of the classical Euler–Bernoulli expressions, which neither account for shear deformation nor rotatory inertia, implying that the theory developed herein applies only to slender beams. The driving point mobility of the bending wave horn (at the free end) is obtained from a matrix inversion. The numerical results are shown in Figure 3, which includes two normalized driving point mobilities (magnitudes), as functions of the Helmholtz number based on the wavenumber k_∞ of the uniform member and the tapered tip length L. The normalization is introduced to obtain results that are independent of both material properties and beam

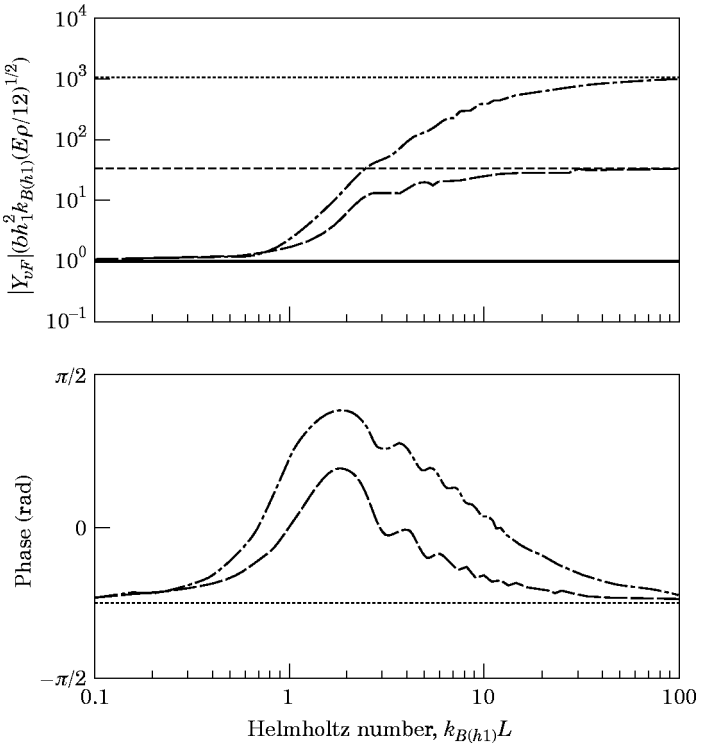

Figure 3. The normalized magnitude (top) and phase (bottom) of force mobility for two bending wave horns with normalized tip heights of $h_0/L = 10^{-2}$ (— —) and $h_0/L = 10^{-3}$ (– · –), with $h_1/L = 10^{-1}$. The normalized force mobilities of uniform prismatic, semi-infinite beams with normalized heights of $h/L = 10^{-1}$ (——), $h/L = 10^{-2}$ (-----) and $h/L = 10^{-3}$ (· · · · · ·).

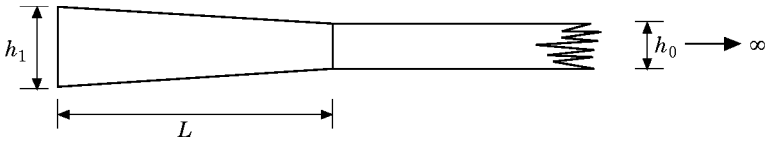

Figure 4. The "inverted" bending wave horn.

width. The two curves refer to bending wave horns which differ only by their depth at the free end, $h_0/L = 10^{-2}$ and $h_0/L = 10^{-3}$ respectively, whereas the depth of the semi-infinite member remains unchanged, at $h_1/L = 10^{-1}$ in both cases. Also included, for reference, are the corresponding mobilities for uniform, semi-infinite prismatic beams.

At low Helmholtz numbers, the bending wave horn driving point mobility coincides with that of the semi-infinite beam as the bending wavelength abundantly exceeds the tip length. At approximately unit Helmholtz number, the curves start to deviate from the infinite beam behaviour, and at high Helmholtz numbers they asymptotically approach the mobilities of semi-infinite beams of depths corresponding to those at their respective free ends. Almost no reflection occurs at the discontinuity, resulting in a very efficient energy transfer from the tapered tip into the semi-infinite member. The modes, the first of which one can be observed in the range of Helmholtz numbers between 2 and 3, consequently appear highly damped, rendering only a slight and smooth ripple. Further analysis shows that the reflection coefficient at the discontinuity is independent of the tapering angle and is a function solely dependent on the ratio h_0/h_1.

For a system that can be termed the "inverted" horn, as depicted in Figure 4, the point force mobility has a somewhat different signature. In Figure 5 is shown the normalized point force mobility for the end position. In this case as well, the normalization is based on the dynamic characteristics of the semi-infinite member. It is observed that, for this configuration, the mobility is essentially mass-governed for small Helmholtz numbers, again based on the height of the semi-infinite part. At Helmholtz numbers just below 0·1, the system exhibits a transition to a second, almost purely mass controlled region. This region prevails up to the point at which roughly half a wavelength for a uniform beam of height h_1 corresponds to the length of the taper and the reflections from the discontinuity begin to interfere with the outgoing waves. The first mass-controlled region is associated with a translational motion of a beam with a tip mass: i.e., the inverted horn can be seen lumped as a mass. In the second, the rotational inertia of the horn, supported by the rotational stiffness of the semi-infinite beam member, realizes the mass character. In the transition from translation to rotation, the point and point–cross mobilities of the beam member are all involved.

2.4. THE SEMI-INFINITE WEDGE: THE BENDING WAVE ACCELERATOR

The semi-infinite wedge discussed in this section is made of a homogeneous isotropic linear elastic material and has a rectangular cross-section with constant width. The depth of the cross section is h_0 at $x = 0$ and it increases in proportion to the longitudinal co-ordinate, as illustrated in Figure 6.

If the beam is excited by a transverse force at the free end, a bending wave will propagate along the beam towards infinity. Since there are no discontinuities, no reflections will occur. While the bending wave propagates along the beam, the phase speed and consequently the wavelength increase proportionally to the square root of the cross-sectional depth. Thus, the greater the distance from the excitation position is, the larger is the ratio of beam depth to wavelength. At large distances from the free end therefore, the bending wave will gradually convert to a shear wave with a constant,

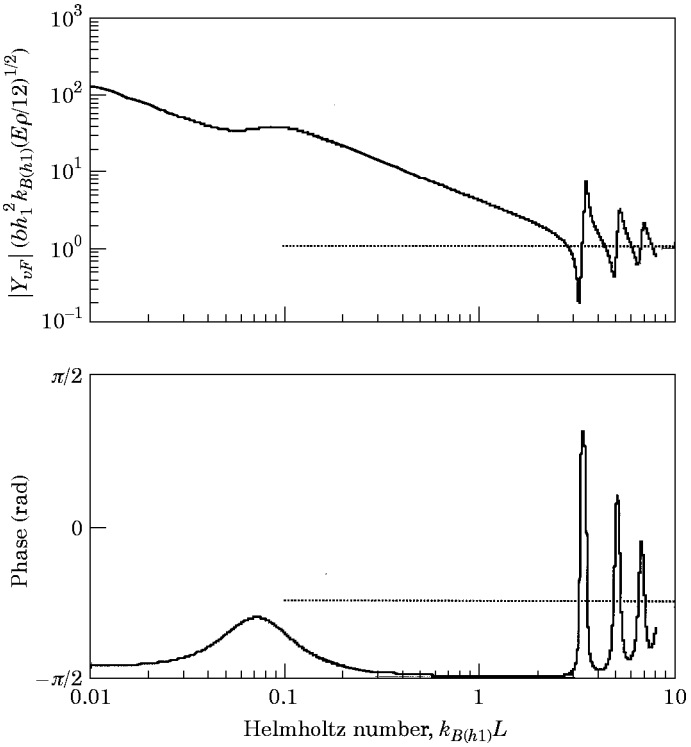

Figure 5. The normalized magnitude (top) and phase (bottom) of force mobility for an "inverted" bending wave horn with normalized height of $h_1/L = 10^{-1}$ (——) at the excited end and $h_0/L = 10^{-3}$. The normalized force mobilities of uniform prismatic, semi-infinite beam with normalized height of $h/L = 10^{-3}$ (· · · · ·).

cross-section independent, phase speed; see, e.g., reference [16]. The amplitude of the wave motion, on the other hand, decreases continuously as the wave advances due to the progressively increasing mass and bending stiffness. In the theoretical analysis presented herein, however, pure bending waves are assumed and shear deformation effects are omitted. The phase speed of the pure bending waves is thus theoretically allowed to increase without bound as the wave propagates along the beam.

In order to find a mathematical description for the pure bending wave field in a semi-infinite wedge the general solution, equation (9), can be rewritten using the relationships between Bessel and Hankel functions:

$$\mathrm{J}_1(2\kappa\sqrt{X}) = \tfrac{1}{2}[\mathrm{H}_1^{(1)}(2\kappa\sqrt{X}) + \mathrm{H}_1^{(2)}(2\kappa\sqrt{X})], \tag{12a}$$

$$\mathrm{Y}_1(2\kappa\sqrt{X}) = -(\mathrm{i}/2)[\mathrm{H}_1^{(1)}(2\kappa\sqrt{X}) - \mathrm{H}_1^{(2)}(2\kappa\sqrt{X})]. \tag{12b}$$

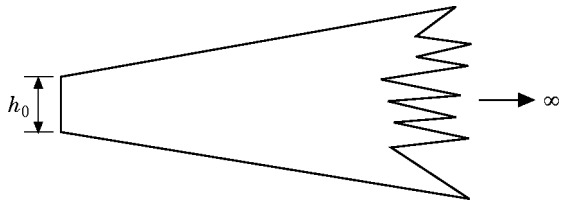

Figure 6. The semi-infinite wedge.

With the time base chosen, the Hankel functions of the first and second kind represent the spatial propagation functions, $\mathrm{H}_1^{(2)}$ being associated with the waves travelling in the positive x-direction and $\mathrm{H}_1^{(1)}$ with waves travelling in the opposite direction. The modified Bessel functions K_1 and I_1, moreover, represent fields with constant phase and can be interpreted as near-field contributions which decrease exponentially in the positive and the negative x-directions respectively. For the semi-infinite wedge, the backwards propagating parts must be discarded under the postulate of no reflections from infinity and consequently the following general solution may be assumed for the velocity field:

$$v(X) = \left(1/\sqrt{X}\right)\left(A\mathrm{H}_1^{(2)}\left(2\kappa\sqrt{X}\right) + B\mathrm{K}_1\left(2\kappa\sqrt{X}\right)\right). \tag{13}$$

Substitution into equation (8) shows that such a field satisfies the general differential equation for tapered beams. A and B are the unknown (frequency dependent) coefficients to be determined from the boundary conditions at the free end. For the transversally force-excited semi-infinite wedge, the remaining boundary conditions are,

$$M_0 = 0, \qquad F_0 = F. \tag{14}$$

From the theory of linear elasticity, compatibility yields

$$M = -\frac{EI}{\mathrm{i}\omega}\frac{\partial^2 v}{\partial x^2} = -\frac{Eb\alpha^2}{12\mathrm{i}\omega}X^3\frac{\partial^2 v}{\partial X^2}, \qquad F = -\frac{\partial M}{\partial x} = \frac{Eb\alpha^3}{12\mathrm{i}\omega}\frac{\partial}{\partial X}\left(X^3\frac{\partial^2 v}{\partial X^2}\right). \tag{15}$$

The unknown coefficients A and B in equation (13) can be formally written as

$$A = \frac{\mathrm{i}12\omega F}{Eb\alpha^3}\frac{2\kappa\sqrt{h_0}\,\mathrm{K}_0\left(2\kappa\sqrt{h_0}\right) + (\kappa^2 h_0 + 2)\mathrm{K}_1\left(2\kappa\sqrt{h_0}\right)}{D},$$

$$B = \frac{\mathrm{i}12\omega F}{Eb\alpha^3}\frac{2\kappa\sqrt{h_0}\,\mathrm{H}_0^{(2)}\left(2\kappa\sqrt{h_0}\right) + (\kappa^2 h_0 - 2)\mathrm{H}_0^{(2)}\left(2\kappa\sqrt{h_0}\right)}{D}, \tag{16}$$

where

$$\begin{aligned} D = {} & 4\kappa^2\sqrt{h_0}\,\mathrm{K}_1\left(2\kappa\sqrt{h_0}\right)\mathrm{H}_1^{(2)}\left(2\kappa\sqrt{h_0}\right) \\ & + 4\kappa^3 h_0\left(\mathrm{K}_0\left(2\kappa\sqrt{h_0}\right)\mathrm{H}_1^{(2)}\left(2\kappa\sqrt{h_0}\right) - \mathrm{K}_1\left(2\kappa\sqrt{h_0}\right)\mathrm{H}_0^{(2)}\left(2\kappa\sqrt{h_0}\right)\right) \\ & - 4\kappa^4 h_0\sqrt{h_0}\,\mathrm{K}_0\left(2\kappa\sqrt{h_0}\right)\mathrm{H}_0^{(2)}\left(2\kappa\sqrt{h_0}\right) \\ & - \kappa^5 h_0^2\left(\mathrm{K}_0\left(2\kappa\sqrt{h_0}\right)\mathrm{H}_1^{(2)}\left(2\kappa\sqrt{h_0}\right) + \mathrm{K}_1\left(2\kappa\sqrt{h_0}\right)\mathrm{H}_0^{(2)}\left(2\kappa\sqrt{h_0}\right)\right). \end{aligned} \tag{17}$$

Together, equations (13), (16) and (17) constitute the closed form expression for the point and transfer mobilities of a semi-infinite wedge subject to transverse force excitation at the free end. In Figure 7 is presented the numerically evaluated normalized point mobility as a function of Helmholtz number $\kappa\sqrt{h_0}$.

For small Helmholtz numbers, the mobility is dominated by the imaginary part, and it is observed that this is stiffness controlled. This can be explained by the fact that for sufficiently small Helmholtz numbers the depth at the free end becomes very small in comparison with the beam depth at, for instance, a quarter wavelength from the end, establishing a cantilever type of behaviour of the tip.

The point mobility magnitude exhibits a broad maximum centred at $\kappa\sqrt{h_0} \approx 1{\cdot}184$ (the estimate is obtained from close inspection of the imaginary part) where the imaginary part

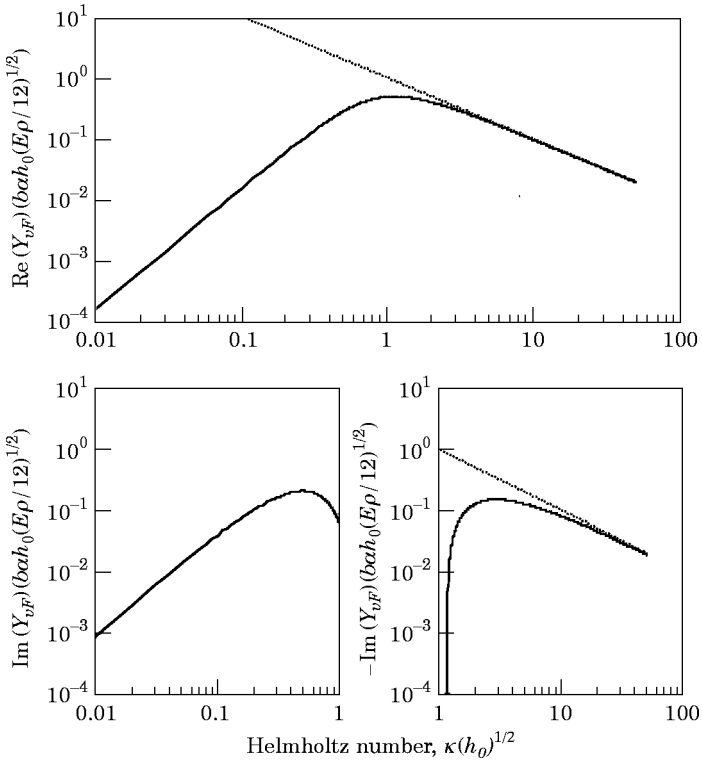

Figure 7. The normalized real and imaginary parts of force mobility at the tip of a semi-infinite wedge. The normalized real and imaginary parts of force mobility of a uniform, semi-infinite prismatic beam of height equal to that of the tip of the semi-infinite wedge (· · · · ·).

changes sign. This means that the system is resonant at

$$f \approx (1{\cdot}4/2\pi)\,(\alpha^2/h_0)\sqrt{E/12\rho}, \tag{18a}$$

reaching a maximum of

$$Y_{res} \approx (1/2b\alpha h_0)\sqrt{12/E\rho}. \tag{18b}$$

At high Helmholtz numbers the mobility of the semi-infinite wedge asymptotically approaches the mass-governed mobility of a semi-infinite prismatic beam with depth h_0, i.e., the depth at the free end.

In Figure 8, the normalized (characteristic) mobility of the semi-infinite wedge is compared with the mobilities of three bending wave horns, again as functions of the Helmholtz number $\kappa\sqrt{h_0}$. The curves for the bending wave horns turn out to be dependent only on the ratio h_1/h_0 and not on the taper angle or tip length. The importance of the derived characteristic mobility lies in the fact that it predicts the global dynamic behaviour of any finite tapered beam in the modal frequency range by providing the mean line through the resonance maxima and the anti-resonance minima. This feature is confirmed in Figure 8 where, above the first tip mode, the characteristic mobility approximates the bending wave horn mobility curves.

In order to gain more insight into the rather involved expression for the characteristic, mobility, it is useful to study the asymptotic behaviour for small and large Helmholtz

numbers. Upon expanding the Bessel functions for small arguments, the asymptotic transfer mobility can be found to be given by

$$Y_{vF}(X) \to \sqrt{\frac{12}{E\rho}}\,\frac{\kappa^2}{b\alpha}\left[\frac{\pi}{2} - 2\mathrm{i}\left(\ln(\kappa\sqrt{X}) + \gamma_E - \tfrac{1}{2} + \frac{h_0}{4X}\right)\right]. \tag{19}$$

Specifically, for the point mobility at the end of the beam, one finds that

$$Y_{vF} \to \frac{1}{b\alpha h_0}\sqrt{\frac{12}{E\rho}}\,(\kappa\sqrt{h_0})^2\left[\frac{\pi}{2} - 2\mathrm{i}\left(\ln(\kappa\sqrt{h_0}) + \gamma_E - \tfrac{1}{4}\right)\right]. \tag{19a}$$

Note that the real part of the mobility, and therefore the power fed into the beam by force excitation, is independent of h_0 at low Helmholtz numbers, whereas the imaginary part has a logarithmic dependence. Reduction of the tip height, for a constant tapering angle, may therefore result in arbitrarily high driving point mobilities while the power remains finite. This may again be explained by the fact that at these low Helmholtz numbers the beam depth "seen" by the propagating wave is much larger than the tip depth; the latter consequently has no significance for the energy but governs the deformation.

The asymptotes for the real and imaginary parts are displayed versus Helmholtz number in Figure 9 together with the numerically evaluated, normalized mobility. It is seen that the expression in equation (19) acceptably depicts the behaviour for Helmholtz numbers below 0·4, at which the real and imaginary parts also are about equal.

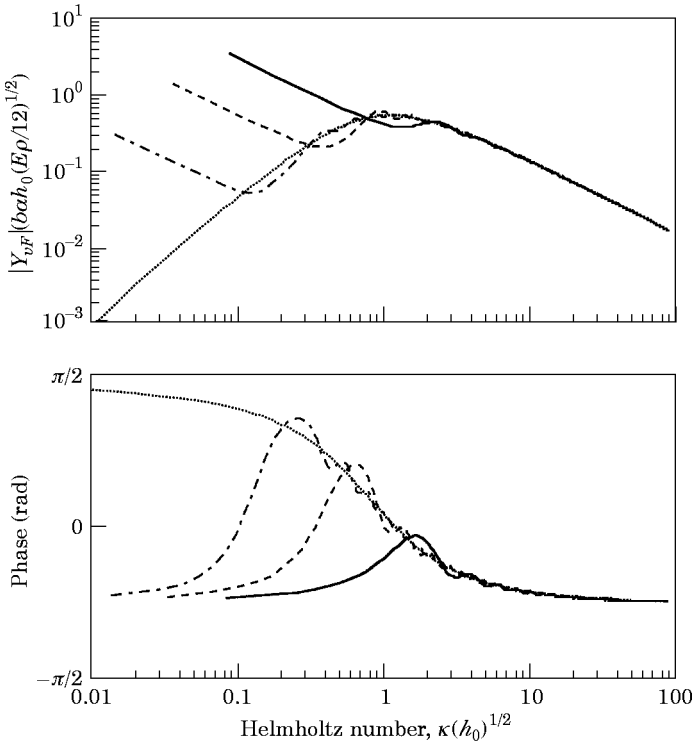

Figure 8. The normalized force mobility of three different bending wave horns: $h_1/h_0 = 3$ (——), $h_1/h_0 = 10$ (----) and $h_1/h_0 = 50$ (– · –). The normalized force mobility of a semi-infinite wedge (· · · · ·).

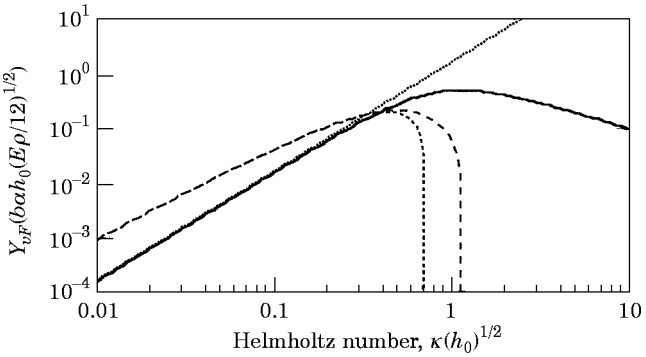

Figure 9. A comparison of first order approximations and numerically evaluated results for the point force mobility at the end of a semi-infinite wedge. ——, Real part; – –, imaginary part. Asymptotic behaviour for small arguments; real (· · · · ·) real and imaginary (-----) parts.

For the other extreme, i.e., when the argument becomes large as, for instance, at high frequencies, the asymptotic behaviour of the transfer mobility is obtained as

$$Y_{vF}(X) \rightarrow \sqrt{\frac{12}{E\rho}}\frac{1}{b\alpha}\frac{(1-\mathrm{i})}{2\kappa\sqrt[4]{(h_0\,X)^3}}(\mathrm{e}^{\mathrm{i}2\kappa(\sqrt{h_0}-\sqrt{X})}+\mathrm{e}^{2\kappa(\sqrt{h_0}-\sqrt{X})})$$

$$=\frac{(1-\mathrm{i})}{2}\sqrt[4]{\frac{12}{E\rho^3}}\frac{1}{b\sqrt[4]{(h_0\,X)^3}}\frac{1}{\sqrt{\omega}}(\mathrm{e}^{\mathrm{i}2\kappa(\sqrt{h_0}-\sqrt{X})}+\mathrm{e}^{2\kappa(\sqrt{h_0}-\sqrt{X})}). \tag{20}$$

This result suggests that the mobility essentially decreases with distance from the tip with a power 3/4 and that it involves an "equivalent" height equal to the geometric mean of the beam heights at the excitation and response positions.

In Figure 10 is shown the variation in transfer mobility magnitude with non-dimensional distance; the positions here correspond to those used in the experimental work.

Specializing on the point force mobility at the end of the beam one finds that, as expected, it approaches that of the corresponding semi-infinite beam of height equal to that at the beam end i.e.,

$$Y_{vF}(x=0) \rightarrow (\omega/B(h_0)k^3_{B(h_0)})(1-\mathrm{i}) \tag{20a}$$

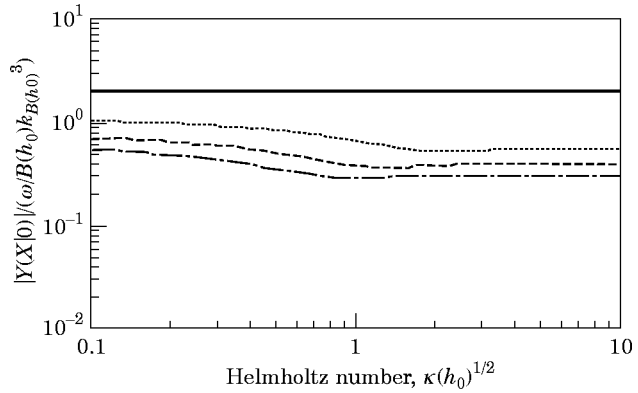

Figure 10. The magnitude of the normalized transfer mobility for some values of X/h_0 and $\alpha = 0{\cdot}08$. ——, $X/h_0 = 1$; · · · · ·, $X/h_0 = 2{\cdot}32$; ----, $X/h_0 = 3{\cdot}64$; – · – · –, $X/h_0 = 4{\cdot}96$.

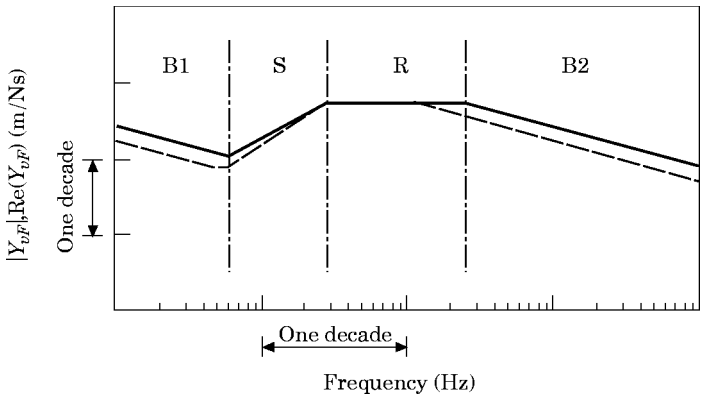

Figure 11. The log–log diagram of the estimated magnitude and real part of the point force mobility at the end of a tapered semi-infinite beam.

Expressions (18), (19) and (20) together with the recognized cantilever type behaviour (cf. Appendix III) allow the development of an estimation procedure for the point mobility of the bending wave horn by using five straight lines (on a log–log scale). The procedure is detailed in Appendix IV and the resulting graph is presented in Figure 11. As is seen, the signatures are almost the same for the magnitude and the real part although the numerical values will differ.

In region B1, the mobility is fully governed by the semi-infinite beam member. For region S, the magnitude is estimated from a cantilevered, tapered finite beam, while the real part has a slightly steeper increase. For small enough depth ratios h_1/h_0, this region will vanish and the mobility follows the real-valued cross-mobility from moment to translatory velocity of the semi-infinite beam member whereby the tapered part is considered as a massless rigid lever. The mobility in the region denoted R is either set to the real-valued maximum established at resonance for the accelerator in cases of large depth ratios or remains constant at the cross-mobility level in cases of small ratios. In region B2, finally, the mobility is that of a uniform beam with a height equal to that at the excited end of the tapered part. Thus, physically acceptable approximations are introduced for the transition region between deep and thin beam behaviour to circumvent the evaluation of the extensive products of Bessel functions.

3. EXPERIMENTS

3.1. EXPERIMENTAL ARRANGEMENTS

To examine the theoretical model established and assess the applicability of the design procedure developed, three series of experiments have been undertaken on a tapered, Perspex beam. In order to gain a clear picture of the interesting transition region between the behaviour of the main beam and that of the corresponding semi-infinite wedge, the 7·1 m long Perspex beam was tapered at both ends with different taper angles, see Figure 12. The small slope of the neutral layer for these non-symmetric tapers is neglected.

The beam was fabricated from four pieces which were glued and tapped together, with the intent to establish a monolithic system. Initially, the material properties of the Perspex used were estimated and the Young's modulus revealed from axial pulse measurements was found to be 5·9 GPa. The density was estimated to be 1200 kg/m^3.

Only bending motion in the plane of the beam length and height has been considered although the cross-mobility to the out-of-plane, translatory response component was assessed to warrant a negligible interference from coupling to torsional motion. For the excitation, a small shaker was attached, via a force transducer, at the end of the beam on the tapered edge. In order to minimize the mass between the force transducer and the measurement object, the pin-screw of the force transducer was fastened directly to the beam by means of wax. Careful adjustment was also undertaken to obtain an excitation perpendicular to the main axis of the beam. The response was registered by means of a miniature accelerometer, also attached with wax but on the opposite, flat edge. Subsequent to conditioning, the excitation and response signals were fed to a multi-channel signal analyzer.

The measurement range was divided into a lower and an upper range with an overlap at about 800 Hz whereby a coherence larger than 0.95 could be achieved overall. Accordingly, the results presented are composed of two sets of measured data joined at the crossover frequency. In the mobility measurements, additional damping was introduced by placing the beam on its side letting approximately two thirds of its length rest on a felt-like carpet. The remaining part of the beam was supported by a few rubber band cradles.

The first series of measurements comprised the point force mobility at the end of the short taper and the second the corresponding quantity at the end of the long taper. In the third series, attempts were made to verify the dependence on distance for the transfer mobility at high frequencies.

3.2. EXPERIMENTAL RESULTS

In Figure 13 are shown the magnitude and phase of the point force mobility at the end of the short taper. As is seen from the diagrams, the main beam fully governs the mobility up to about 100 Hz above which there is a smooth transition towards a mobility initially governed by that of the semi-infinite wedge and subsequently by that of a semi-infinite beam with a beam height corresponding to that at the actual tip. By applying the "accelerator" resonance criterion, equation (18a), the maximum of the transition region for the object considered is obtained at 507 Hz, which is close to that observed in the measured results.

One may note that the phase, which according to the theoretical model should converge to $-\pi/4$ in the upper range, actually exhibits a continuous decrease.

The behaviour of the mobility in the upper part of the frequency range considered and the presumed convergence to the mobility of the semi-infinite wedge is more clearly displayed in Figure 14, where the point force mobility at the end of the long taper is presented. With this taper angle, the maximum of the transition region would be at 45 Hz based on the "accelerator" resonance criterion, an effect which, however, is only weakly indicated in the experimental results. Above the maximum (for this taper) the mobility principally has the slope of that of a semi-infinite wedge in most of the experimental range. In the uppermost part of the frequency range, the measured results starts to deviate from

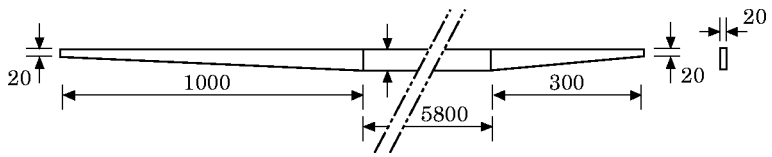

Figure 12. A sketch showing the dimensions (in mm) of the tapered Perspex beam used in the experiments.

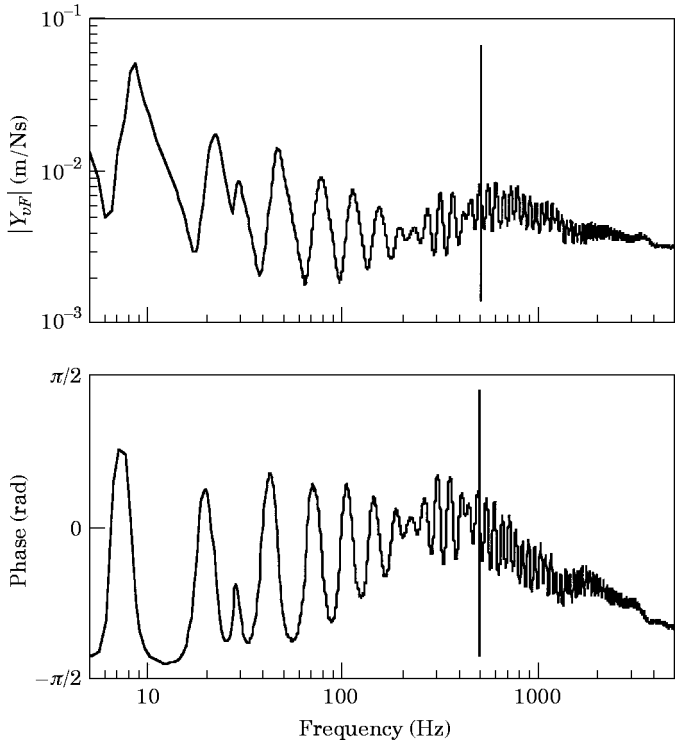

Figure 13. The magnitude and phase of the point mobility of a tapered beam at the end of the short taper. The calculated frequency for the maximum of the transition region and the phase alternation is indicated.

those of the model and an increased slope of the magnitude is indicated. The deviation is evident from the phase curve where the tendency is towards that of a mass controlled mobility for frequencies above 2 kHz. This is to be expected, since for very high frequencies at which the wavelength becomes comparable with the height of the beam—in this case the height of the main beam—Euler–Bernoulli theory is no longer applicable, but shear deformation comes into play. A closer scrutiny of the real and imaginary parts shown in Figures 15 and 16 for the two tapers, respectively, reveals the marked decrease of the real part, while the imaginary slowly approaches that of the purely bending, semi-infinite beam. This also explains the trend of the phase towards that of a mass.

It is seen that while the real part is consistently below the asymptote developed (i.e., the real part of the mobility of a semi-infinite beam of height equal to that of the end of the actual beam), the imaginary part tends towards its asymptote. The same behaviour is exhibited for the long taper, where the additional feature of a staircase-shaped decrease of the real part is less pronounced. A careful comparison reveals, however, that although the real parts are slightly different, the overall signature and the periodicity are the same.

The observed discrepancies between the theoretical and experimental results mean that a model based upon Euler–Bernoulli theory will have an upper limit of validity, which in accordance with that of a uniform beam can be set to $\lambda_B > 6h$ or, equivalently, $f < (\pi/18h)\sqrt{E/12\rho}$. For the experimental configuration, the limit is approximately 1100 Hz as set by the main beam. It is worth noting that the corresponding limit for a beam of height equal to that of the tip is about 5600 Hz. Accordingly, a taper implies that as well as a temporally governed transition to shear there is also a spatial one.

For a system such as the one considered experimentally, consisting of a linearly tapered beam and a finite uniform part, the asymptotic behaviour of the real part can be understood by considering a model of a finite undamped beam attached to a one-dimensional shear wave guide. The real part of the mobility of such a model asymptotically will be inversely proportional to the frequency, which is in agreement with the experimental results at high frequencies. Naturally, the transition to the "mass-loaded shear waveguide" behaviour will be gradual.

Yet another aspect that also affects the comparisons at high frequencies is the practical difficulty in realizing an excitation precisely at the beam end, as well as registering the response there. As a consequence, the fraction of the tip that is beyond the cross-sectional plane of the transducers forms an end mass. This mass, although small, will add to the inevitable mass-loading caused by the instrumentation; the latter, however, being taken into account and corrected for.

Upon introducing a rigid indenter in the excitation arrangement to examine a possible influence of the stress distribution and local deformation, the real part of the mobility at the end of the long taper, corrected for the mass of the indenter, is slightly altered as shown in Figure 17. In this diagram, the signature is less regular than that in Figure 16 and pronounced troughs can be seen. Above 1 kHz, the deviation from slender beam theory is evident. The overall trend, however, is in agreement with that of the real part measured with the pin-screw of the force transducer directly attached to the beam.

It is also worthwhile to compare the numerical results obtained from the model with the experimental ones. In Figures 18 and 19 are shown the real and imaginary parts for the short and long tapers respectively. It can be observed that while the model gives results

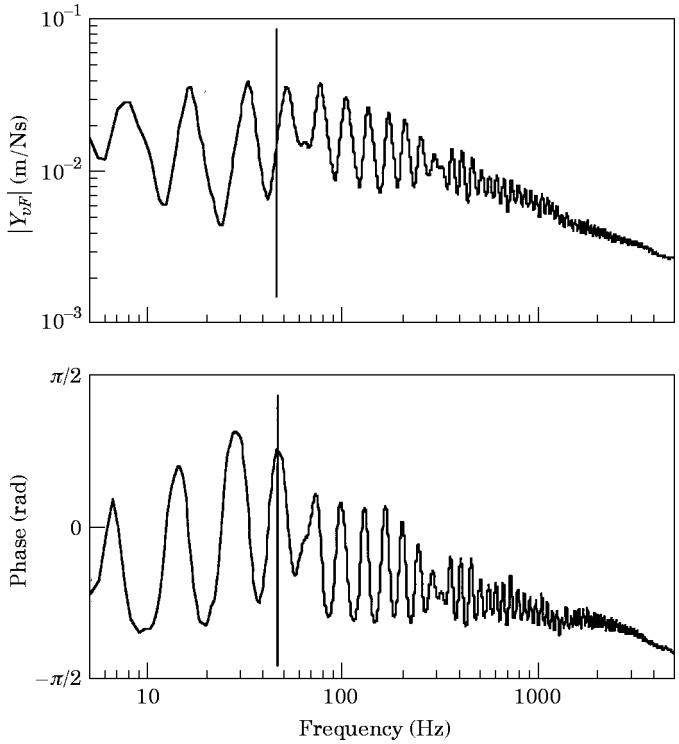

Figure 14. The magnitude and phase of the point mobility of a tapered beam at the end of the long taper. The calculated maximum of the transition region and the phase alternation is indicated.

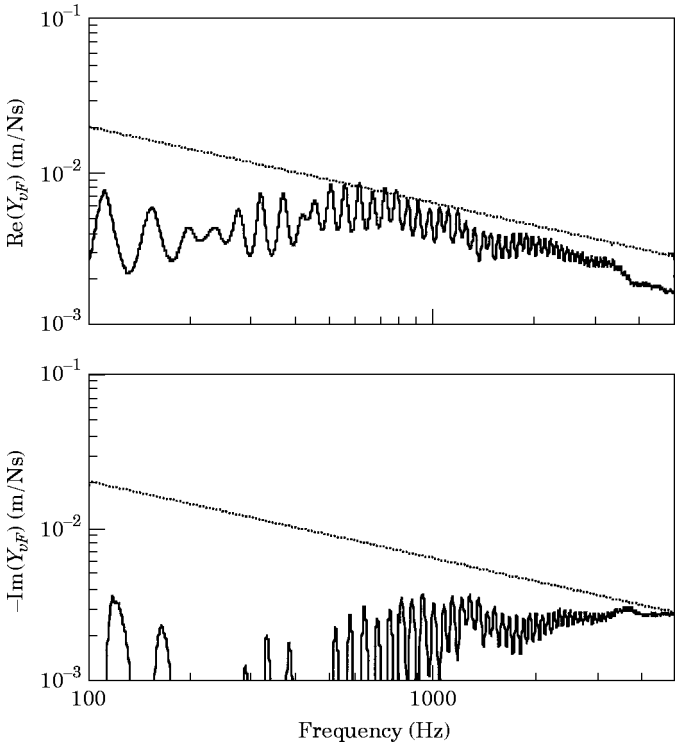

Figure 15. The real and imaginary parts of the point mobility of a tapered beam at the end of the short taper. Assumed asymptotic behaviour indicated.

that are in agreement with measurements in the range in which Euler–Bernoulli theory is valid, the deviations are marked in the region above. Furthermore, upon comparing the results for the short and long taper, it appears that the modulation due to the interference from reflections at the discontinuity between the tapered and the uniform parts in the case of a short taper realizes a phase shift that is different from that of the model. Since the taper angle is larger at this end than at the end with the long taper, the sensitivity to the exact response position is enhanced and a small shift in the experiments may explain the discrepancies.

In Figure 20 are shown the magnitudes of the point and two transfer mobilities, measured at the long taper. The transfer mobilities were obtained with the response positions at $x = 0{\cdot}33$ m and $x = 0{\cdot}66$ m respectively. Also included are the associated transfer mobilities estimated from the semi-infinite wedge model in equation (20).

It is seen that while both the asymptotic behaviour of the semi-infinite wedge and the experimental results for the uniform beam with a tapered end demonstrate marked and the same decreases with distance, calculated results are consistently overestimating the magnitudes. In an attempt to explain this difference, one may compare with calculated results using the complete expressions. Such a comparison is presented in Figure 21, where it is confirmed that the numerical results from the complete model gradually deviate from the experimental ones the further away the response position and the same overestimation as obtained with the high frequency asymptote is established numerically in the upper frequency range. This means that calculations based on the approximate expressions developed herein from slender beam theory will yield conservative results.

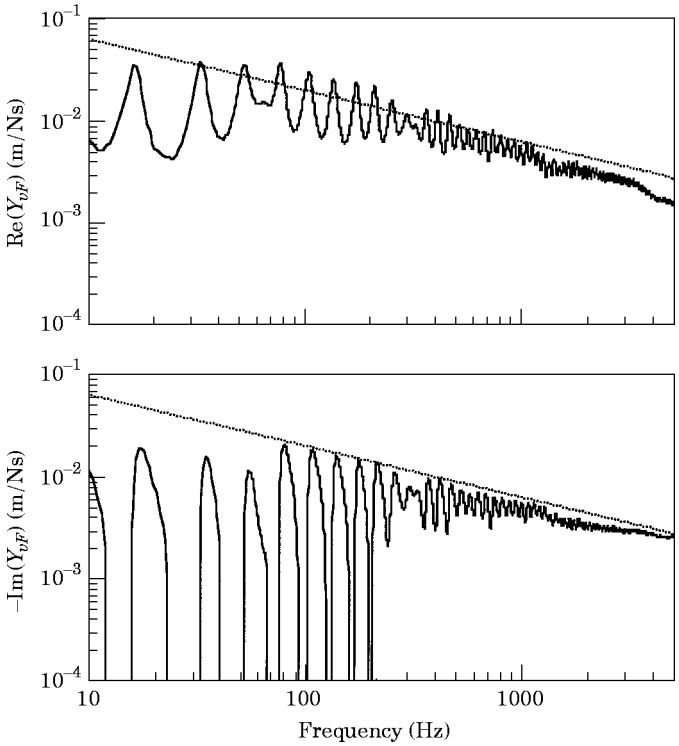

Figure 16. The real and imaginary parts of the point mobility of a tapered beam at the end of the long taper. Assumed asymptotic behaviour indicated.

The applicability of the estimation procedure proposed is explored in Figure 22. The top diagram shows the measured magnitude of the mobility overlaid on the results obtained by using the estimation procedure and the bottom diagram the corresponding data for the real part. It is observed that with the exception of region B2 (see Figure 11), the estimation procedure captures the signatures of the magnitude as well as the real part. This corroborates its applicability within the range of validity of Euler–Bernoulli theory.

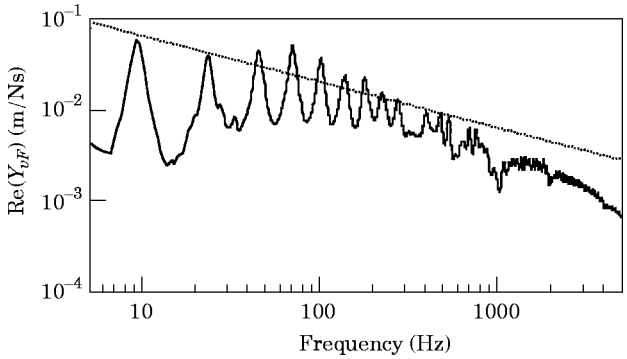

Figure 17. The real part of point mobility of a tapered beam measured with a rigid indenter of length equal to the width of the beam at the end of the long taper. Assumed asymptotic behaviour indicated.

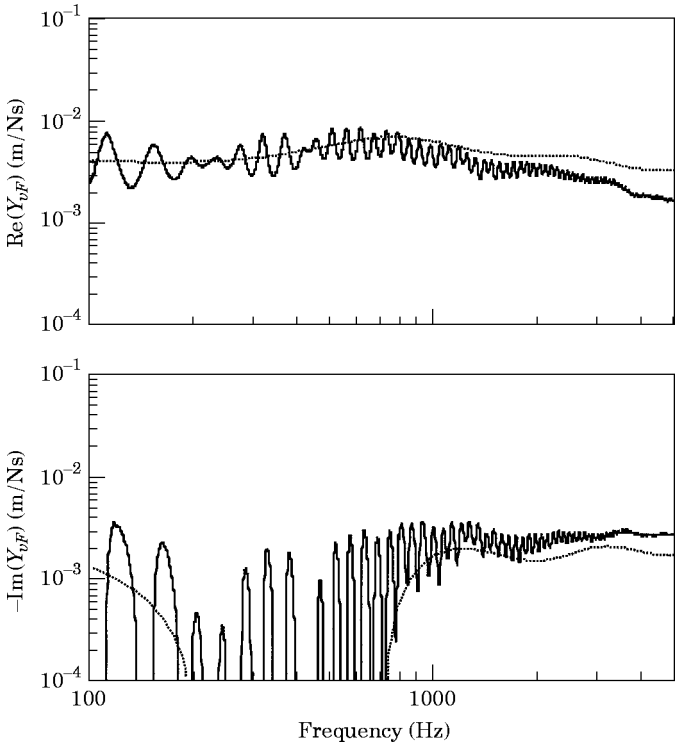

Figure 18. A comparison of measured (——) and numerically evaluated (· · · · ·) point force mobilities at the end of the short taper.

4. CONCLUDING REMARKS

The study shows that spatially varying properties of a one-dimensional waveguide can markedly alter its vibration as well as transmission characteristics. It is further evident that, for the theoretically important semi-infinite case also, resonant behaviour is realized. From the analysis of the influence of tapering on the dynamic characteristics of the flexural wave counterpart to the acoustic horn, it is found that the main distinction to the uniform case is the comparatively broad-banded transition from flexural vibrations governed by the properties of the deep part of the system to flexural vibrations governed by those of the slender part. Here, it should be noted that a structural transformation from a deep to a slender section is phenomenologically different from that of slender to deep. This means that, for small Helmholtz numbers, the one-dimensional horn configuration can be treated as a uniform beam of dimensions corresponding to those at the deep end, while for large Helmholtz numbers, the slender end geometry yields the corresponding uniform beam. The intermediate transition region is featured by a stiffness-controlled initial part, followed by a resonant part. In contrast, the "inverted" horn configuration exhibits an essentially mass-controlled transition region between, in this case asymptotically, slender beam behaviour for small Helmholtz numbers and deep beam behaviour for large. Furthermore, the transition itself involves a transition from mainly translational to rotational motion of the tapered part. Moreover, in contrast to the wave propagation in the uniform case, the wave amplitude for a tapered beam is proven to be dependent on the separation between the excitation and response positions. From the asymptotic behaviour for large Helmholtz numbers, one may conclude that the transfer mobility is primarily influenced by the geometrical mean of the heights at the two ends of the taper. It should

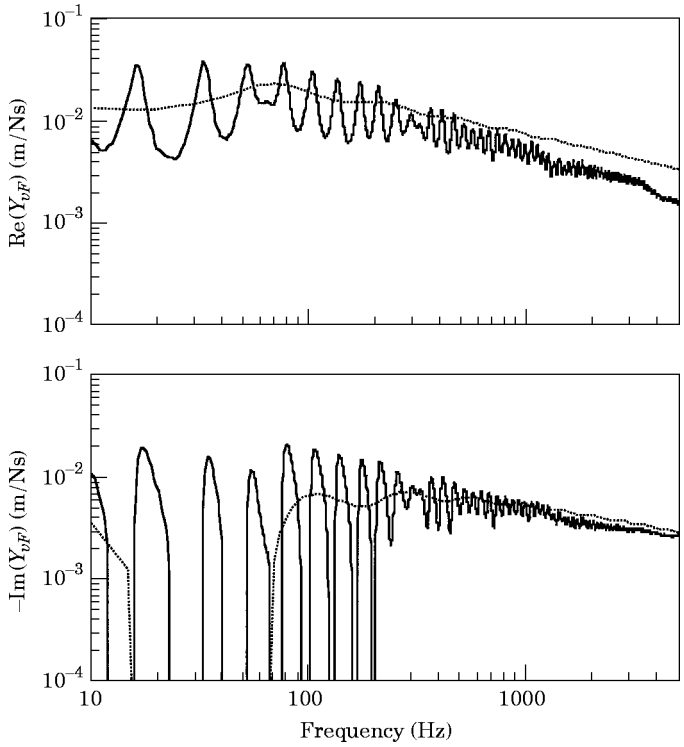

Figure 19. A comparison of measured (——) and numerically evaluated (· · · · ·) point force mobilities at the end of the long taper.

be emphasized that all of the analysis is based on Euler–Bernoulli theory, which will restrict the applicability to frequencies for which the deep beam can be considered in pure bending.

From the analysis of the semi-infinite wedge—"the bending wave accelerator"–it can be inferred that the transition region established in the horn case also comprises a taper shape dependent resonance on which, in the finite case, are superimposed the constructive and destructive interferences due to reflections from the discontinuity between the two structural members. Such a shape dependent resonance can be explained from the

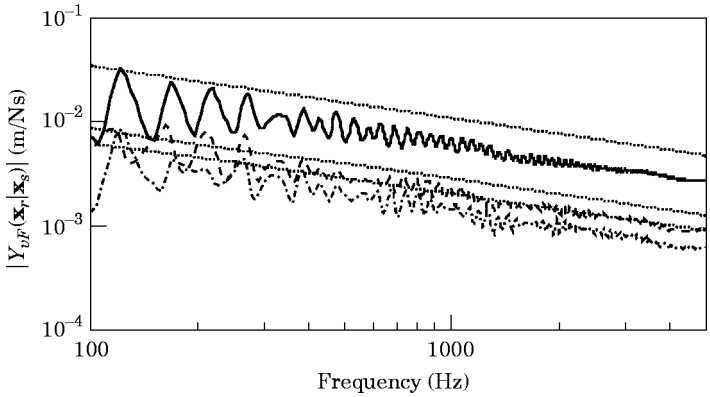

Figure 20. The measured magnitudes of the transfer mobility at long taper. ——, $|x_r - x_s| = 0$; -----, $|x_r - x_s| = 0{\cdot}33$ m; – · – · –, $|x_r - x_s| = 0{\cdot}66$ m; · · · · ·, asymptotic behaviour according to equation (20).

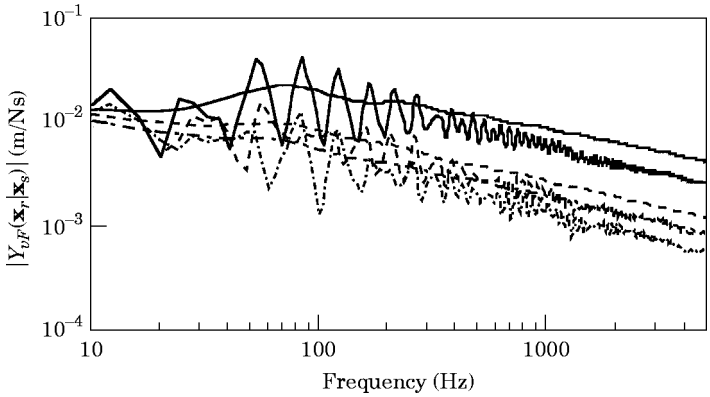

Figure 21. Computed and measured transfer mobilities. ——, $|x_r - x_s| = 0$; ----, $|x_r - x_s| = 0{\cdot}33$ m; – · – · –, $|x_r - x_s| = 0{\cdot}66$ m.

mass–spring system constituted by the mass moment of inertia of a portion of the taper and the rotational stiffness of the remaining part of the semi-infinite wedge.

The experimental results obtained for a system made up of a tapered and a uniform beam not only show that the model for a tapered, semi-infinite beam accurately describes the dynamic behaviour but, foremost, confirm the applicability of the asymptotic expressions developed, thus demonstrating the reliability of the parameter dependence

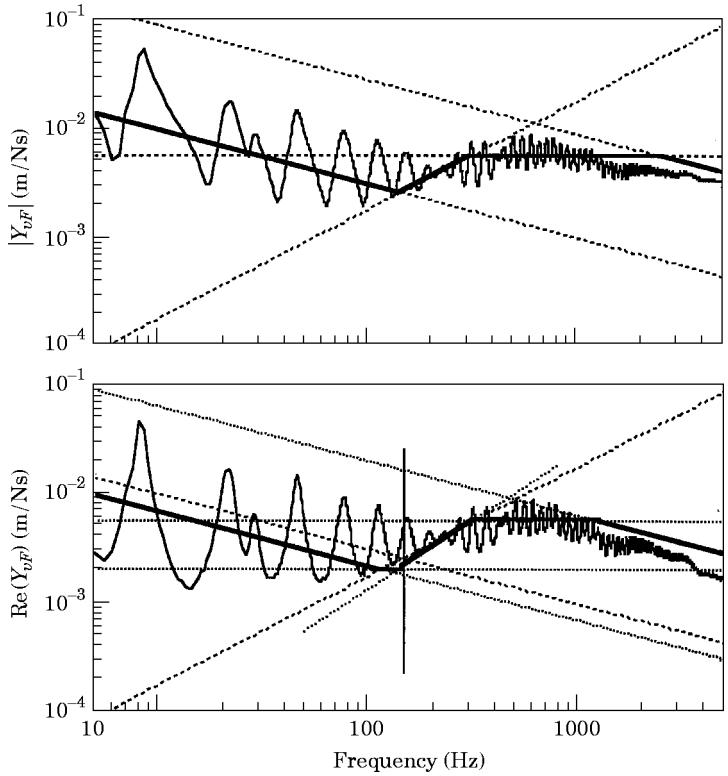

Figure 22. A comparison of the measured (——) and estimated (——) point force mobility at the end of the short taper. Generating lines for magnitude (- - - - - - -) and the real part (· · · · ·).

extracted. Moreover, from the experiments it is clear that the region of validity is that set by negligible influence of shear deformation of the beam lamina. This means that the estimation procedure proposed correctly depicts the dynamic characteristics of the bending wave horn in the same region.

In a design perspective, the employment of spatially varying properties such as linearly varying height for beam-like structures can be interesting owing to savings with respect to cost, weight and space. The introduction of a broad resonance controlled transition region, however, markedly limits the usefulness from a vibration transmission point of view. As a rule of thumb, therefore, such designs should be considered only for Helmholtz numbers, $k_{B(h_1)} L$, well below unity.

REFERENCES

1. L. Cremer 1948 *Department of Scientific and Industrial Research*, *Report no*.1, *series* B. The propagation of structure-borne sound.
2. R. H. Lyon and R. G. deJong 1995 *Theory and Application of Statistical Energy Analysis*. Boston: Butterworth–Heinemann; second edition.
3. E. Skudrzyk 1980 *Journal of the Acoustical Society of America*, **67**, 1105–1135. Mean-value method of predicting the dynamic response of complex vibrators.
4. J. M. Garrelick 1987 *Journal of the Acoustical Society of America*, **81**, 1979–1982. The error in a narrow-band transfer function model prediction.
5. M. Heckl 1961 *BBN Report No*. 774. Compendium of impedance formulas.
6. B. Petersson and J. Plunt 1982 *Journal of Sound and Vibration* **82**, 531–540. On effective mobilities for the prediction of structure-borne sound transmission between a source structure and a receiving structure; part II: procedures for the estimation of mobilities.
7. U. J. Kurze 1985 *Zeitschrift für Lärmbekämpfung*, **32**, 126–134. Einige Ergänzungen zur VDI-Richtlinie 370, Bl. 6: Lärmarm konstruieren—Mechanische Impedanzen.
8. B. A. T. Petersson 1993 *Proceedings of the International Conference on Noise and Vibration Control*, *St*. *Petersburg*, **2**, 31–36. System definition for structure-borne sound and vibration transmission analysis.
9. B. A. T. Petersson 1994 *Proceedings of Noise-Con*, *Fort Lauderdale*, 585–590. A T-frame for analysis of structure-borne sound transmission by multi-point and component excitation.
10. D. L. Karabalis and D. E. Beskos 1983 *Computers and Structures* **16**, 731–748. Static, dynamic and stability analysis of structures composed of tapered beams.
11. S. Naguleswaran 1992 *Journal of Sound and Vibration* **172**, 289–304. A direct solution for the transverse vibration of Euler–Bernoulli wedge and cone beams.
12. A. P. Gupta and N. Goyal 1994 *Journal of Sound and Vibration* **174**, 461–474. Effect of transverse shear and rotatory inertia on the forced motion of a plate-strip of linearly varying thickness.
13. C. W. Bert and M. Malik 1996 *Journal of Sound and Vibration* **190**, 41–63. Free vibration analysis of tapered rectangular plates by differential quadrature method: a semi-analytical approach.
14. E. T. Cranch and A. A. Adler 1956 *Journal of Applied Mechanics* **23**, 103–108. Bending vibrations of variable section beams.
15. V. Kolousek 1973 *Dynamics in Engineering Structures*. London: Butterworth.
16. L. Cremer, M. Heckl and E. Ungar 1973 *Structure-borne Sound*. Berlin: Springer-Verlag.

APPENDIX I: ELEMENTS OF THE IMPEDANCE MATRIX FOR A FINITE TAPERED BEAM

The following closed form expressions were derived for the elements of the impedance matrix in equation (10) (see also Figure 1),

$$Z_{00}^{Fv} = -\mathrm{i}(Eb\alpha^3/6\omega)\,(D_1/T), \qquad Z_{01}^{Fv} = \mathrm{i}(Eb\alpha^3/6\omega)\,(D_2/T),$$

$$Z_{10}^{Mv} = -\mathrm{i}(Eb\alpha^2/6\omega)\,(D_3/T), \qquad Z_{00}^{Mw} = -\mathrm{i}(Eb\alpha/6\omega)\,(h_0^2 + D_4/T),$$

$$Z_{10}^{Mw} = \mathrm{i}(Eb\alpha/6\omega)\,(D_5/T), \qquad Z_{00}^{Mv} = \mathrm{i}(Eb\alpha^2/6\omega)\,(D_6/T),$$

$$Z_{11}^{Fv} = \mathrm{i}(Eb\alpha^3/6\omega)\,(D_7/T), \qquad Z_{11}^{Mw} = \mathrm{i}(Eb\alpha/6\omega)\,(h_1^2 + D_8/T),$$

$$Z_{11}^{Mv} = -\mathrm{i}(Eb\alpha^2/6\omega)\,(D_9/T), \qquad Z_{10}^{Fw} = -\mathrm{i}(Eb\alpha^2/6\omega)\,(D_{10}/T).$$

The functions D_1–D_{10} and T are given below. A short notation is used for the Bessel functions (the subscript refers to the order of the Bessel function, whereas the superscript refers to the arguments of the Bessel functions), for example, $K_0^0 = K_0(2\kappa\sqrt{h_0})$, while $K_0^1 = K_0(2\kappa\sqrt{h_1})$. With these abbreviations,

$$\begin{aligned}
T = \{&-I_0^1 J_0^0 K_1^0 Y_1^1 + I_1^1 J_0^0 K_1^0 Y_0^1 + I_0^1 J_1^1 K_1^0 Y_0^0 - I_0^0 J_1^1 K_1^0 Y_0^1 - I_1^1 J_0^0 K_1^0 Y_0^0 + I_0^0 J_0^1 K_1^0 Y_1^1 \\
&- I_1^0 J_0^0 K_0^1 Y_1^1 - I_1^0 J_0^0 K_1^1 Y_0^1 + I_1^0 J_1^1 K_0^1 Y_0^0 - I_1^0 J_1^1 K_0^0 Y_0^1 + I_1^0 J_0^1 K_1^1 Y_0^0 + I_1^0 J_0^1 K_0^0 Y_1^1 \\
&+ I_0^1 J_0^0 K_1^1 Y_1^0 + I_1^1 J_0^0 K_0^1 Y_1^0 - I_0^0 J_1^1 K_0^1 Y_1^0 + I_0^1 J_1^1 K_0^0 Y_1^0 - I_1^1 J_0^1 K_0^0 Y_1^0 - I_0^0 J_0^1 K_1^1 Y_1^0 \\
&- I_1^1 J_0^0 K_1^0 Y_0^1 - I_0^1 J_1^0 K_1^1 Y_0^0 + I_0^0 J_1^0 K_0^1 Y_1^1 - I_0^1 J_1^0 K_0^0 Y_1^1 + I_0^0 J_1^0 K_1^1 Y_0^1 + I_1^1 J_1^0 K_0^0 Y_0^1\}, \\
D_1 = (\kappa\sqrt{h_0})\{&-I_1^0 J_1^0 K_0^1 Y_1^1 - I_0^1 J_1^0 K_1^0 Y_1^1 - I_1^0 J_1^0 K_1^1 Y_0^1 + I_1^1 J_1^0 K_1^0 Y_0^1 + I_1^0 J_1^1 K_0^1 Y_0^1 \\
&+ I_0^1 J_1^1 K_1^0 Y_1^0 + I_1^0 J_0^1 K_1^1 Y_1^0 - I_1^1 J_0^1 K_1^0 Y_1^0\} \\
&+ (\kappa\sqrt{h_0})^2\{-I_1^0 J_0^1 K_1^1 Y_0^0 + I_1^0 J_0^0 K_0^1 Y_1^1 + I_0^0 J_1^0 K_0^1 Y_1^1 - I_0^1 J_1^0 K_0^0 Y_1^1 + I_0^1 J_0^0 K_1^0 Y_1^1 \\
&+ I_0^0 J_1^0 K_1^1 Y_1^0 + I_1^0 J_0^0 K_1^1 Y_1^0 + I_1^1 J_0^0 K_0^1 Y_1^0 - I_1^1 J_0^0 K_1^0 Y_0^1 - I_1^0 J_1^1 K_0^1 Y_0^0 - I_0^0 J_1^1 K_0^1 Y_1^0 \\
&+ I_0^1 J_1^1 K_0^0 Y_1^0 - I_0^1 J_1^1 K_1^0 Y_0^0 - I_0^0 J_0^1 K_1^1 Y_1^0 - I_1^1 J_0^1 K_0^0 Y_1^0 + I_1^1 J_0^1 K_1^0 Y_0^0\} \\
&+ (\kappa\sqrt{h_0})^3\{ + I_0^0 J_0^1 K_1^1 Y_0^0 - I_0^0 J_0^0 K_0^1 Y_1^1 + I_0^1 J_0^0 K_0^0 Y_1^1 - I_0^0 J_0^0 K_1^1 Y_0^1 \\
&- I_1^1 J_0^0 K_0^0 Y_1^1 + I_0^0 J_1^1 K_0^1 Y_0^0 + I_1^1 J_0^1 K_0^0 Y_0^0 - I_0^1 J_1^1 K_0^0 Y_0^0\}, \\
D_2 = \kappa^3 h_1\sqrt{h_0}\{&+ I_1^1 J_0^1 K_0^1 Y_0^0 + I_1^1 J_0^1 K_1^1 Y_0^0 - I_0^0 J_0^1 K_0^1 Y_1^1 + I_0^1 J_0^1 K_0^0 Y_1^1 \\
&- I_0^1 J_0^0 K_1^1 Y_0^1 - I_1^1 J_0^0 K_0^1 Y_0^1 + I_0^0 J_1^1 K_0^1 Y_0^1 - I_0^1 J_1^1 K_0^0 Y_0^1\} \\
&+ \kappa^2\sqrt{h_1}\sqrt{h_0}\{-I_1^1 J_1^1 K_0^1 Y_0^0 - I_0^1 J_1^1 K_1^1 Y_0^0 + I_0^0 J_1^1 K_1^1 Y_0^1 + I_1^1 J_1^1 K_0^0 Y_0^1 \\
&+ I_0^1 J_0^0 K_1^1 Y_1^1 + I_1^1 J_0^0 K_0^1 Y_1^1 - I_1^1 J_0^1 K_0^0 Y_1^1 - I_0^0 J_0^1 K_1^1 Y_1^1\} \\
&+ \kappa^2 h_1\{-I_1^1 J_0^1 K_0^1 Y_1^0 - I_0^1 J_0^1 K_1^1 Y_1^0 + I_1^0 J_0^1 K_0^1 Y_1^1 + I_0^1 J_0^0 K_1^1 Y_1^1 \\
&+ I_0^1 J_1^0 K_1^1 Y_0^1 + I_1^1 J_1^0 K_0^1 Y_0^1 - I_1^0 J_1^1 K_0^1 Y_0^1 - I_0^1 J_1^1 K_1^0 Y_0^1\} \\
&+ \kappa\sqrt{h_1}\{ + I_1^1 J_1^1 K_0^1 Y_1^0 + I_0^1 J_1^1 K_1^1 Y_1^0 - I_1^0 J_1^1 K_1^1 Y_0^1 + I_1^1 J_1^1 K_1^0 Y_0^1 \\
&- I_0^1 J_1^0 K_1^1 Y_1^1 - I_1^1 J_1^0 K_0^1 Y_1^1 - I_1^1 J_0^1 K_1^0 Y_1^1 + I_1^0 J_0^1 K_1^1 Y_1^1\}, \\
D_3 = \kappa^2 h_1\sqrt{h_1}\sqrt{h_0}\{&+ I_1^1 J_1^1 K_0^1 Y_0^0 + I_0^1 J_1^1 K_1^1 Y_0^0 - I_0^0 J_1^1 K_1^1 Y_0^1 - I_1^1 J_1^1 K_0^0 Y_0^1 \\
&- I_0^1 J_0^0 K_1^1 Y_1^1 - I_1^1 J_0^0 K_0^1 Y_1^1 + I_1^1 J_0^0 K_1^0 Y_1^1 + I_0^0 J_0^1 K_1^1 Y_1^1\} \\
&+ \kappa h_1\sqrt{h_1}\{-I_1^1 J_1^1 K_0^1 Y_1^0 - I_0^1 J_1^1 K_1^1 Y_1^0 + I_1^0 J_1^1 K_1^1 Y_0^1 - I_1^1 J_1^1 K_1^0 Y_0^1 \\
&+ I_0^1 J_1^0 K_1^1 Y_1^1 + I_1^1 J_1^0 K_0^1 Y_1^1 + I_1^1 J_0^1 K_1^0 Y_1^1 - I_1^0 J_0^1 K_1^1 Y_1^1\},
\end{aligned}$$

$$D_4 = \kappa h_0^2 \sqrt{h_0}\{-I_1^0 J_1^0 K_0^1 Y_1^1 - I_0^1 J_1^0 K_1^0 Y_1^1 - I_1^0 J_1^0 K_1^1 Y_0^1 + I_1^1 J_1^0 K_1^0 Y_0^1$$
$$+ I_1^0 J_1^1 K_0^1 Y_1^0 + I_0^1 J_1^1 K_1^0 Y_1^0 + I_1^0 J_0^1 K_1^1 Y_1^0 - I_1^1 J_0^1 K_1^0 Y_1^0\},$$

$$D_5 = \kappa h_0 h_1 \sqrt{h_1}\{I_1^1 J_1^1 K_0^1 Y_1^0 + I_0^1 J_1^1 K_1^1 Y_1^0 - I_1^0 J_1^1 K_1^1 Y_0^1 + I_1^1 J_1^1 K_1^0 Y_0^1$$
$$- I_1^1 J_1^0 K_0^1 Y_1^1 - I_0^1 J_1^0 K_1^1 Y_1^1 + I_1^0 J_0^1 K_1^1 Y_1^1 - I_1^1 J_0^1 K_1^0 Y_1^1\},$$

$$D_6 = \tfrac{1}{2}\kappa^2 h_0^2\{+I_1^1 J_1^0 K_0^1 Y_0^0 + I_0^1 J_1^0 K_1^1 Y_0^0 - I_0^0 J_1^0 K_0^1 Y_1^1 + I_0^1 J_1^0 K_0^0 Y_1^1$$
$$- I_0^0 J_1^0 K_1^1 Y_0^1 - I_1^1 J_1^0 K_0^0 Y_0^1 - I_0^1 J_0^0 K_1^1 Y_1^0 - I_1^1 J_0^0 K_0^1 Y_1^0$$
$$+ I_0^0 J_1^1 K_0^1 Y_1^0 - I_0^1 J_1^1 K_0^0 Y_1^0 + I_1^1 J_0^1 K_0^0 Y_1^0 + I_0^0 J_0^1 K_1^1 Y_1^0$$
$$- I_1^0 J_0^0 K_0^1 Y_1^1 - I_1^0 J_0^0 K_1^1 Y_0^1 + I_1^0 J_1^1 K_0^1 Y_0^0 - I_1^0 J_1^1 K_0^0 Y_0^1$$
$$+ I_1^0 J_0^1 K_1^1 Y_0^0 + I_1^0 J_0^1 K_0^0 Y_1^1 - I_0^1 J_0^0 K_1^0 Y_1^1 + I_1^1 J_0^0 K_1^0 Y_0^1$$
$$+ I_0^1 J_1^1 K_1^0 Y_0^0 - I_0^0 J_1^1 K_1^0 Y_0^1 - I_1^1 J_0^1 K_1^0 Y_0^0 + I_0^0 J_0^1 K_1^0 Y_1^1\}$$
$$+ \kappa h_0 \sqrt{h_0}\{ + I_1^0 J_1^0 K_0^1 Y_1^1 + I_0^1 J_1^0 K_1^0 Y_1^1 + I_1^0 J_1^0 K_1^1 Y_0^1 - I_1^1 J_1^0 K_1^0 Y_0^1$$
$$- I_1^0 J_1^1 K_0^1 Y_1^0 - I_0^1 J_1^1 K_1^0 Y_1^0 + I_1^1 J_0^1 K_1^0 Y_1^0 - I_1^0 J_0^1 K_1^1 Y_1^0\},$$

$$D_7 = \kappa^2 h_1\{-I_1^0 J_0^1 K_1^1 Y_0^0 - I_1^0 J_0^0 K_0^1 Y_1^1 + I_0^0 J_1^0 K_0^1 Y_1^1 - I_0^1 J_1^0 K_0^0 Y_1^1$$
$$- I_0^1 J_0^0 K_1^0 Y_1^1 - I_0^0 J_1^1 K_1^1 Y_0^1 + I_1^1 J_0^0 K_1^1 Y_0^1 - I_1^1 J_1^0 K_0^0 Y_0^1$$
$$- I_1^1 J_0^0 K_1^0 Y_0^1 + I_1^0 J_1^1 K_0^1 Y_0^0 - I_0^0 J_1^1 K_0^1 Y_1^0 + I_0^1 J_1^1 K_0^0 Y_1^0$$
$$+ I_0^1 J_1^1 K_1^0 Y_0^0 + I_0^0 J_0^1 K_1^1 Y_1^0 + I_1^1 J_0^0 K_1^0 Y_1^0 + I_1^1 J_0^1 K_1^0 Y_0^0\}$$
$$+ \kappa^3 h_1 \sqrt{h_1}\{-I_0^1 J_0^1 K_0^0 Y_1^1 + I_0^1 J_0^0 K_1^0 Y_1^1 + I_0^0 J_0^1 K_1^0 Y_1^1 - I_0^1 J_0^1 K_1^0 Y_0^0$$
$$- I_1^0 J_0^1 K_0^1 Y_0^0 + I_0^1 J_1^0 K_0^0 Y_1^1 + I_1^0 J_0^1 K_0^0 Y_1^1 - I_0^0 J_1^0 K_0^1 Y_1^1\}$$
$$+ \kappa\sqrt{h_1}\{-I_1^1 J_1^1 K_0^0 Y_1^0 - I_0^0 J_1^1 K_1^1 Y_1^0 - I_1^1 J_1^1 K_1^0 Y_1^0 + I_1^0 J_1^1 K_1^1 Y_0^0$$
$$+ I_1^1 J_1^0 K_0^0 Y_1^1 + I_0^0 J_1^0 K_1^1 Y_1^1 + I_1^1 J_0^0 K_1^0 Y_1^1 - I_1^0 J_0^0 K_1^1 Y_1^1\},$$

$$D_8 = \kappa h_1^2 \sqrt{h_1}\{-I_1^1 J_1^1 K_0^0 Y_1^0 - I_0^0 J_1^1 K_1^1 Y_1^0 - I_1^1 J_1^1 K_1^0 Y_0^0 + I_1^0 J_1^1 K_1^1 Y_0^0$$
$$+ I_1^1 J_1^0 K_0^0 Y_1^1 + I_0^0 J_1^0 K_1^1 Y_1^1 + I_1^1 J_0^0 K_1^0 Y_1^1 - I_1^0 J_0^0 K_1^1 Y_1^1\},$$

$$D_9 = \tfrac{1}{2}\kappa^2 h_1^2\{+I_1^0 J_1^1 K_0^0 Y_0^1 + I_0^0 J_1^1 K_1^0 Y_0^1 - I_1^0 J_1^1 K_0^0 Y_1^0 + I_0^0 J_1^1 K_0^0 Y_1^1$$
$$- I_0^1 J_1^1 K_1^0 Y_0^0 - I_1^1 J_1^1 K_0^1 Y_0^0 - I_0^0 J_0^1 K_1^1 Y_1^0 - I_1^0 J_0^1 K_0^1 Y_1^1$$
$$+ I_0^1 J_1^0 K_0^0 Y_1^1 - I_0^0 J_1^0 K_1^1 Y_1^1 + I_1^0 J_0^1 K_0^0 Y_1^1 + I_0^1 J_0^0 K_1^0 Y_1^1$$
$$- I_1^1 J_0^1 K_0^0 Y_1^0 - I_1^1 J_0^0 K_1^1 Y_0^0 + I_1^1 J_1^0 K_0^0 Y_0^1 - I_1^1 J_1^0 K_1^0 Y_0^0$$
$$+ I_1^1 J_0^0 K_1^0 Y_1^1 + I_1^1 J_0^0 K_0^1 Y_1^0 - I_0^0 J_0^1 K_1^1 Y_1^0 + I_1^0 J_0^1 K_1^1 Y_0^0$$
$$+ I_0^0 J_1^1 K_1^1 Y_0^0 - I_1^0 J_1^1 K_1^1 Y_0^0 - I_1^0 J_0^0 K_1^1 Y_1^0 + I_1^0 J_0^0 K_1^1 Y_1^0\}$$
$$+ \kappa h_1 \sqrt{h_1}\{ + I_1^1 J_1^1 K_0^0 Y_1^0 + I_0^0 J_1^1 K_1^1 Y_1^0 + I_1^1 J_1^1 K_1^0 Y_0^0 - I_1^0 J_1^1 K_1^1 Y_0^0$$
$$- I_1^1 J_1^0 K_0^0 Y_1^1 - I_0^0 J_1^0 K_1^1 Y_1^1 + I_1^0 J_0^0 K_1^1 Y_1^1 - I_1^1 J_0^0 K_1^0 Y_1^1\},$$

$$D_{10} = \kappa^2 h_0 h_1 \{ + I_1^1 J_0^1 K_0^1 Y_1^0 + I_0^1 J_0^1 K_1^1 Y_1^0 - I_1^0 J_0^1 K_0^1 Y_1^1 - I_0^1 J_0^1 K_1^0 Y_1^1$$
$$- I_0^1 J_1^0 K_1^1 Y_0^1 - I_1^1 J_1^0 K_0^1 Y_0^1 + I_1^0 J_1^1 K_0^1 Y_0^1 + I_0^1 J_1^1 K_1^0 Y_0^1 \}$$
$$+ \kappa h_0 \sqrt{h_1} \{ - I_1^1 J_1^1 K_0^1 Y_1^0 - I_0^1 J_1^1 K_1^1 Y_1^0 + I_1^0 J_1^1 K_1^1 Y_0^1 - I_1^1 J_1^1 K_1^0 Y_0^1$$
$$+ I_0^1 J_1^0 K_1^1 Y_1^1 + I_1^1 J_1^0 K_0^1 Y_1^1 + I_1^1 J_0^1 K_1^0 Y_1^1 - I_1^0 J_0^1 K_1^1 Y_1^1 \}.$$

APPENDIX II: IMPEDANCE ELEMENTS FOR SMALL TAPER ANGLES

For a very small taper angle—that is, $h_0 \approx h_1 = h$—α tends towards zero and consequently κ grows very large (see equation (9b)). The arguments of the Bessel functions in Appendix I therefore become very large and a good approximation may be achieved by replacing the different Bessel functions by their asymptotic expressions. For the driving point force impedance Z_{00}^{Fv} such a substitution results in the formula,

$$Z_{00}^{Fv} = \frac{Eb\alpha^2}{12} \left\{ -2\left(\frac{12\rho}{E}\right)^{1/2} \frac{h_0}{\alpha} \frac{\sinh[A]\sin[A]}{\cosh[A]\cos[A] - 1} \right.$$
$$- 2\left(\frac{12\rho}{E}\right)^{3/4} \frac{h_0\sqrt{h_0}}{\alpha^2} \sqrt{\omega} \frac{\cosh[A]\sin[A] + \sinh[A]\cos[A]}{\cosh[A]\cos[A] - 1}$$
$$\left. + \left(\frac{12\rho}{E}\right)^{1/4} \frac{\sqrt{h_0}}{\sqrt{\omega}} \frac{\cosh[A]\sin[A] + \sinh[A]\cos[A]}{\cosh[A]\cos[A] - 1} \right\},$$

with $A = 2\kappa(\sqrt{h_1} - \sqrt{h_0})$. For $h_0 \approx h_1 = h$ and α tending to zero this means

$$Z_{00}^{Fv} = \frac{Bk_b^3}{\omega} \frac{\cosh[k_b L]\sin[k_b L] + \sinh[k_b L]\cos[k_b L]}{\cosh[k_b L]\cos[k_b L] - 1},$$

with k_b the wavenumber of a beam with height h, which is identical to the well-known Kolousek function for the point impedance of a homogeneous prismatic beam.

APPENDIX III: STIFFNESSES FOR FINITE TAPERED BEAMS

From the closed form expressions for the impedances, the following asymptotes for small Helmholtz numbers have been derived, which establishes satisfactory approximations for almost all of the range of the depth ratios, h_0/h_1, less than unity (for the three

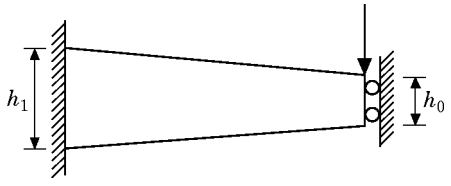

Figure AIII.1. A clamped–guided finite tapered beam.

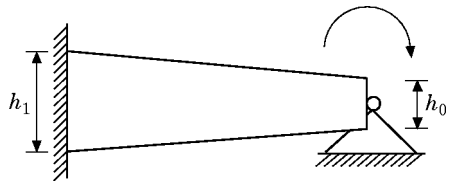

Figure AIII.2. A clamped–simply supported finite tapered beam.

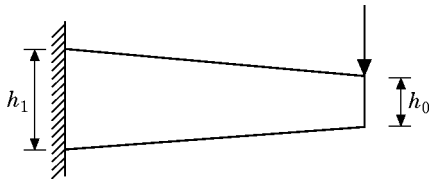

Figure AIII.3. A clamped–free finite tapered beam.

expressions, see, respectively, Figures AIII.1, AIII.2 and AIII.3):

$$s_{c-g} = \frac{Eb\alpha^3}{12}\frac{h_0^2 - h_1^2}{2(h_1 - h_0)^2 + (h_0^2 - h_1^2)\ln(h_1/h_0)};$$

$$s_{c-ss} = \frac{Eb\alpha}{12}\frac{h_0^2[h_0^2 + 3h_1^2 - 4h_1 h_0 - 2h_1^2 \ln(h_1/h_0)]}{2(h_1 - h_0)^2 + (h_0^2 - h_1^2)\ln(h_1/h_0)};$$

$$s = \frac{Eb\alpha^3}{12}\frac{2h_1^4[-2 + \ln(h_1/h_0)] - 2h_0^2 h_1^2[2 + \ln(h_1/h_0)] + 8h_0 h_1^3}{\left\{\begin{array}{c} h_1^4[6 - 7\ln(h_1/h_0) + 2\ln^2(h_1/h_0)] + 2h_0^2 h_1^2[12 - \ln(h_1/h_0) - \ln^2(h_1/h_0)] \\ + h_0^4[2 + \ln(h_1/h_0)] - h_0^3 h_1[12 + 4\ln(h_1/h_0)] + h_0 h_1^3[-20 + 12\ln(h_1/h_0)] \end{array}\right\}}.$$

APPENDIX IV: ESTIMATION PROCEDURE FOR POINT FORCE MOBILITY OF BENDING WAVE HORN

The basic assumptions are linearly elastic, homogeneous material, rectangular cross-section, constant width and linear taper.

AIV.1. MAGNITUDE

Region B1: deep beam behaviour:

$$|Y| = \sqrt{2}/(bh_1\sqrt{h_1}\sqrt[4]{\tfrac{1}{12}E\rho^3}\sqrt{\omega}).$$

Region S: stiffness controlled behaviour: from Appendix III, the compliance of the clamped–free beam tip is given by

$$C = \frac{12}{Eb\alpha^3}\frac{\left\{\begin{array}{c} h_1^4[6 - 7\ln(h_1/h_0) + 2\ln^2(h_1/h_0)] + 2h_0^2 h_1^2[12 - \ln(h_1/h_0) - \ln^2(h_1/h_0)] \\ + h_0^4[2 + \ln(h_1/h_0)] - h_0^3 h_1[12 + 4\ln(h_1/h_0)] + h_0 h_1^3[-20 + 12\ln(h_1/h_0)] \end{array}\right\}}{2h_1^4[-2 + \ln(h_1/h_0)] - 2h_0^2 h_1^2[2 + \ln(h_1/h_0)] + 8h_0 h_1^3},$$

and the mobility in this region becomes

$$|Y| = \omega C.$$

Region R: resonant region: the mobility in this region is calculated from the bending wave accelerator, or the cross-mobility of the semi-infinite beam: i.e.,

$$|Y| = \left\{ \begin{array}{ll} \dfrac{1}{2b\alpha h_0}\sqrt{\dfrac{12}{E\rho}}, & 2C\alpha\left(\dfrac{Ebh_0}{12\rho}\right)^{1/3} > 1 \\ \dfrac{L}{bh_1^2}\sqrt{\dfrac{12}{E\rho}}, & 2C\alpha\left(\dfrac{Ebh_0}{12\rho}\right)^{1/3} \leqslant 1 \end{array} \right\}.$$

Region B2: thin beam behaviour:

$$|Y| = \frac{\sqrt{2}}{bh_0\sqrt{h_0}\sqrt[4]{(\mathrm{E}\rho^3/12)}\sqrt{\omega}}.$$

AIV.2. REAL PART

Region B1: deep beam behaviour:

$$\mathrm{Re}\,[Y] = \left\{ \begin{array}{ll} \dfrac{1}{bh_1\sqrt{h_1}\sqrt[4]{(E\rho^3/12)}\sqrt{\omega}}, & k_{B_1} L < 1 \\ (L/bh_1^2)\sqrt{(12/E\rho)}, & k_{B_1} L \geqslant 1 \end{array} \right\}.$$

Region S: stiffness-controlled behaviour: if $L\sqrt[3]{\sqrt{2}/B_1 C} \leqslant 1$,

$$\mathrm{Re}[Y] = \left\{ \begin{array}{ll} \dfrac{1}{bh_1\sqrt{h_1}\sqrt[4]{(E\rho^3/12)}\sqrt{\omega}}, & \left(\dfrac{\sqrt{2}L^3}{B_1 C}\right)^{1/3} \leqslant k_{B_1} L \leqslant 1 \\ \dfrac{\sqrt{(12/E\rho)}(L/bh_1^2)}{[(h_1/L^2)\sqrt{(E/12\rho)}]^\gamma}\omega^\gamma, & \gamma = \dfrac{-\ln\,[2(1-h_0/h_1)\,(h_0/h_1)]}{\ln\,[6L^3/CEbh_1^3\,(1-h_0/h_1)\,(h_0/h_1)]} \end{array} \right\},$$

whereas, for $L\sqrt[3]{\sqrt{2}/B_1\,\mathrm{C}} > 1$,

$$\mathrm{Re}[Y] = \left\{ \begin{array}{ll} (L/bh_1^2)\sqrt{(12/E\rho)}, & 1 \leqslant k_{B_1} L \leqslant (\sqrt{2}L^3/B_1 C)^{1/3} \\ \dfrac{\sqrt{(12/E\rho)}(L/bh_1^2)}{[(1/h_1)\,(48/C^4b^4E\rho^3)^{1/6}]^\gamma}\omega^\gamma, & \gamma = \dfrac{-\ln\,[2(1-h_0/h_1)\,(h_0/h_1)]}{\ln\,[(3/4CEb)^{1/3}\,L/h_1\,(1-h_0/h_1)\,(h_0/h_1)]} \end{array} \right\},$$

Region R: resonant region:

$$\mathrm{Re}[Y] = \left\{ \begin{array}{ll} (1/2b\alpha h_0)\sqrt{(12/E\rho)}, & 2\alpha(CEb/12)^{1/3} > 1 \\ (L/bh_1^2)\sqrt{(12/E\rho)}, & 2\alpha(CEb/12)^{1/3} \leqslant 1 \end{array} \right\},$$

Region B2: thin beam behaviour:

$$\mathrm{Re}[Y] = 1/(bh_0\sqrt{h_0}\sqrt[4]{(E\rho^3/12)}\sqrt{\omega}).$$

APPENDIX V: SYMBOLS AND NOTATION

B bending stiffness
C compliance
D denominator
F force
$H_n^{(m)}$ Hankel function of order n, mth kind
I moment of inertia of beam cross section area
I_n modified Bessel function of order n
J_n Bessel function of order n
K_n modified Bessel function of order n
L taper length
M moment
V transverse velocity field
X beam depth
Y_n Bessel function of order n
Z impedance
b beam width
h_0 tip height
i imaginary unit
k bending wavenumber
m' mass per unit of length
v translational velocity
w rotational velocity
x axial co-ordinate
α tangent of taper angle
ρ density
ω angular frequency

indices
b beam
r receiver
s source